Annals of Biomedical Engineering (2025) 53:2828–2844
https://doi.org/10.1007/s10439-025-03834-8

BMES BIOMEDICAL ENGINEERING SOCIETY

ORIGINAL ARTICLE

Optimized FDA Blood Pump: A Case Study in System-Level Customized Ventricular Assist Device Designs

Canberk Yıldırım[1] · Kağan Uçak[2] · Ali Madayen[3] · Tansu Gölcez[1] · Hakan Ertürk[4] · Özgür Uğraş Baran[3] · Kerem Pekkan[2]

Received: 10 April 2025 / Accepted: 20 August 2025 / Published online: 9 September 2025
© The Author(s) 2025

Abstract

Purpose The design and development of ventricular assist devices have heavily relied on computational tools, particularly computational fluid dynamics (CFD), since the early 2000s. However, traditional CFD-based optimization requires costly trial-and-error approaches involving multiple design cycles. This study aims to propose a more efficient VAD design and optimization framework that overcomes these limitations.

Methods We developed a system- and component-level ventricle assist device optimization approach by coupling a lumped parameter cardiovascular physiology model with parametric turbomachinery, volute design, and blade path generation packages. The framework incorporates pump hydrodynamic losses and is validated against experimental data from six distinct blood pump designs and CFD simulations. The optimization framework allows for the specification of both physiology-related and device-related objective functions to generate optimized blood pump configurations over a large parameter space.

Results The optimization was applied to the U.S. Food and Drug Administration (FDA) benchmark blood pump as the baseline design. Results showed that an optimized FDA pump, maintaining the same cardiac output and aortic pressure, achieved a ~ 32% reduction in blade tip velocity compared to the baseline, resulting in an ~ 88% reduction in hemolysis. Additionally, an alternative design with a 40% reduction in blood-wetted area was generated while preserving the baseline pressure and flow.

Conclusion The proposed optimization framework improves device development efficiency by shortening the design cycle and enabling hydrodynamically optimized pumps that perform well across diverse patient hemodynamics. The optimized pump designs are available as open-source resources for further research and development.

Keywords Ventricle assist devices · Optimization · Computational fluid dynamics · Lumped parameter modeling · Benchmark devices · FDA blood pump · Cardiovascular engineering

Introduction

State-of-the-art ventricle assist device (VAD) design and optimization primarily rely on computational fluid dynamics (CFD) studies. Studies available in literature were conducted to improve the pump designs in terms of pressure head, pump flow, efficiency, and hemolysis performance by iteratively changing the blade parameters, such as thickness, inlet/outlet angle, wrap angle, splitters, and tip clearance [1–5]. These investigations usually utilized a trial-and-error approach based on a considerable number of design cycles and required multiple CFD runs to reach the desired design specifications. Alternatively, several researchers integrated CFD with optimization algorithms to test a wider range of design alternatives with less computational cost and time, to satisfy hydrodynamic and hemolysis objectives [6–10].

Associate Editor Ender A. Finol oversaw the review of this article.

Canberk Yıldırım, Kağan Uçak, Ali Madayen, Tansu Gölcez and Kerem Pekkan are *HeartWise* European Innovation Council (EIC) Transition project consortium.

✉ Kerem Pekkan
kpekkan@ku.edu.tr

[1] Department of Biomedical Engineering, Koc University, 34060 Istanbul, Turkey

[2] Department of Mechanical Engineering, Koc University, Rumeli Feneri Campus, Sarıyer, 34450 Istanbul, Turkey

[3] Department of Mechanical Engineering, Middle East Technical University, 06800 Ankara, Turkey

[4] Department of Mechanical Engineering, Bogazici University, 34342 Istanbul, Turkey

However, none of these studies include all the design parameters; generally only blade parameters or main impeller dimensions are aimed at being optimized in CFD. Therefore, a new design framework which includes the lumped parameter model (LPM) as a preliminary design tool, and CFD for detailed investigation is proposed in this study.

Although, there are available LPM-based pump design models in literature [11–13], they mainly focused on satisfying the required pump head and flow rate through extremely simple pump design modules. For example, current 1D models rely on the empirical quadratic [14, 15] or linear [16, 17] pump characteristic equations, which limit the number of VAD design parameters that are considered in device optimization. Additionally, these studies typically optimized only for steady design point conditions with constant pressure and flow, can experience altered hemocompatibility under time-periodic, physiological conditions. This highlights the importance of frameworks, which enable optimization under dynamic and hemodynamically realistic boundary conditions, addressing a crucial gap in current pump design practices. To overcome these limitations, a physiology-coupled system-level pump design tool was developed as described in this paper. The proposed design process allows key cardiovascular hemodynamics to be integrated into the optimization process through novel objective functions. Furthermore, it utilizes the full Euler turbomachinery equation for pump modeling, nozzle/volute design and blade path generation which automatically computes the pump characteristic curves for any choice of design parameters without the need for empirical data.

The widespread adoption of CFD in VAD design and optimization has raised concerns about the credibility of CFD results in high-risk clinical decision-making [18]. Therefore, the U.S. Food and Drug Administration (FDA) researchers and collaborators developed a novel benchmark centrifugal blood pump [19], to standardize CFD studies considered for VADs by providing reliable validation datasets. This pump has been further investigated in literature in terms of CFD hemolysis, hydrodynamic performance [20–22] and performed particle image velocimetry (PIV) experiments [23]. Besides providing significant data for hydrodynamic and hemolytic performance of FDA pump, these studies revealed that it lacks a smooth hydrodynamic operation at design and creates a higher blood damage environment due to its simple design and several hydrodynamically unoptimized geometrical features. Thus, as another aim of this study, our team decided to re-visit FDA benchmark critically and optimize its volute, blades, impeller, inlet, nozzle, and shroud in a comprehensive manner using the optimization tool we introduce here, which leverages a patient-specific, target-based cardiovascular lumped parameter model (LPM) to guide pump design.

We hypothesized that the proposed framework would lead to significant improvements in pump performance by broadening the optimization concept through a system-level pump design tool, which can optimize both VAD geometric parameters and in the future can incorporate peripheral circulation specifications like vascular adaptation and remodeling. This tool was tested to present an alternative FDA pump with improved hydrodynamic and hemolytic performance. Our results showed that, the developed tool is promising to be a strong candidate for the preliminary optimized design step that typically takes place before the detailed CFD design effort, by offering physiology couple without multiscale modeling and reducing the trial-and-error optimization steps.

Materials and Methods

The design framework incorporates a clinically validated cardiovascular LPM and an Euler turbomachinery model including impeller and volute design, and blade path generator. All these analysis components are fully coupled with an optimization routine introduced in Fig. 1. The following sections include the details of the LPM, optimization procedure, and the proposed pump design tool.

Lumped Parameter Left Ventricle Failure Circulation Model

Our previous neonatal congenital heart disease [24] and Fontan circulatory lumped parameter (LPM) solver [15] are modified to investigate an adult left ventricle (LV) failure patient with *in silico*-implanted FDA pump as an LVAD. LV failure is simulated in the model for the *'acute state'* by modifying the LV chamber compliance in the LPM, which leads to a decrease in stroke volume and ejection fraction (EF). In this study, coronary circulation and left/right pulmonary circulation branches were added to the recent version of our model as well. Fig. 1 demonstrates the developed LPM network for mechanically assisted LV failure circulation.

FDA Pump Modeling

For the parametric pump modeling, an explicit form of Euler's turbomachinery equation (Eq. 1) is utilized via pump inlet and outlet velocity triangles [25]. In comparison, current literature, including our previous pump studies [14, 15], utilize quadratic-tuned or empirical blood pump characteristic curves as pump equations, which limits the

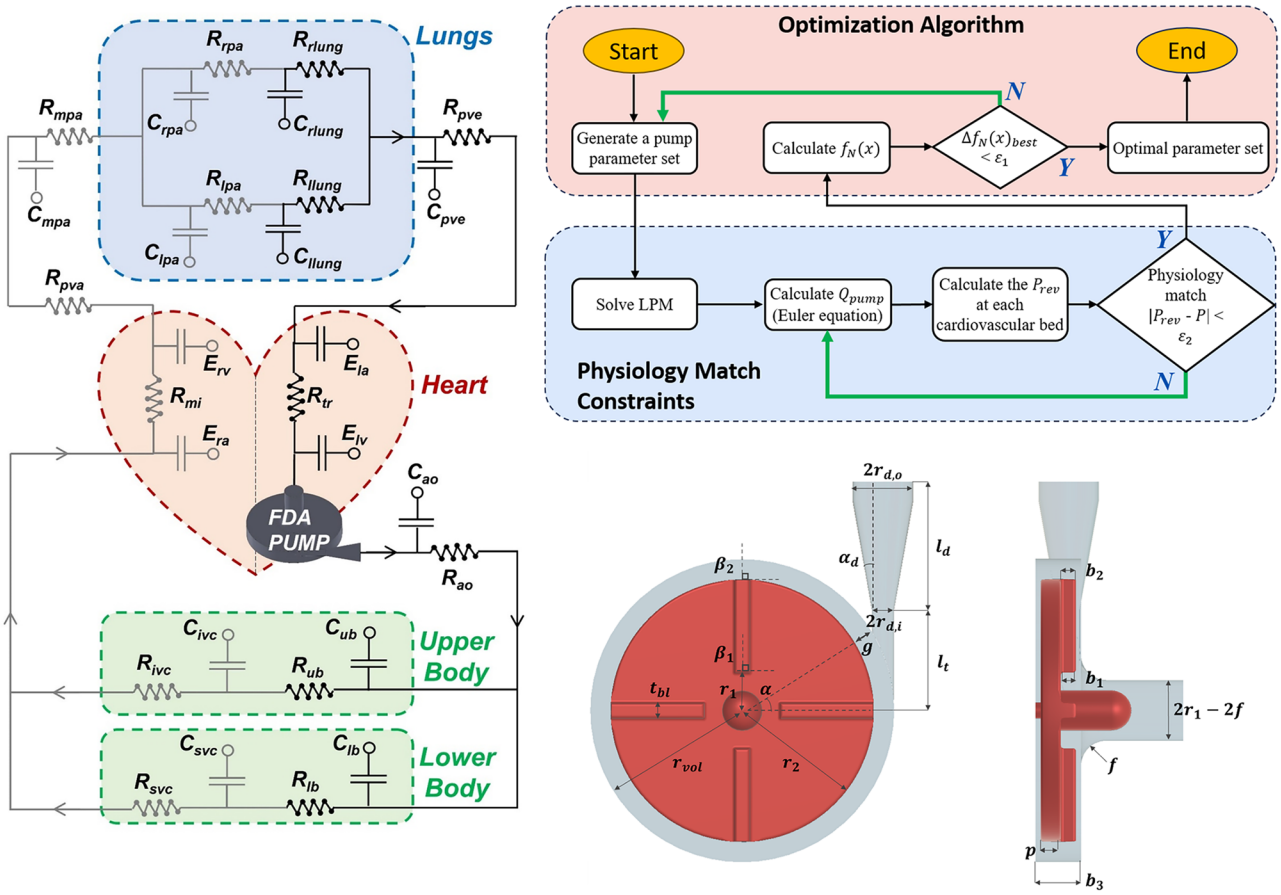


Fig. 1 ***Left***: Established LPM of the FDA pump-implanted biventricle circulation. *C* represents compliance, *E* represents elastance, and *R* is the resistance. Subscripts stand for; lv left ventricle, la left atrium, rv right ventricle, ra right atrium, mi mitral valve, tr tricuspid valve, ao aorta, ub upper body, lb lower body, ivc inferior vena cava, svc superior vena cava, pva pulmonic valve, mpa main pulmonary artery, rpa right pulmonary artery, lpa left pulmonary artery body, llung left lung, rlung right lung, pve pulmonary venous. ***Right***: Optimization and physiology match algorithms developed for optimal pump design. P_{rev}: revised pressure of each compliance chamber with pump operation at the current iteration. *P*: pressure of each compliant chamber at the previous iteration. ε_2: convergence value $\left(\frac{P_{AO,healthy}}{1e5}\right)$ for pump-physiology match. $\Delta f_N(x)_{best}$: best normalized objective function for each generation of genetic algorithm. ε_1: convergence value (1e−6) for optimization. Design parameter set to be optimized. r_1 impeller inlet radius, r_2 impeller outlet radius, t_{bl} blade thickness, z_{bl} blade number, $r_{d,i}$ diffuser inlet radius, $r_{d,o}$ diffuser outlet radius, l_d diffuser length, l_t throat length, b_1 blade inlet width, b_2 blade outlet width, b_3 volute width, β_1 blade inlet angle, β_2 blade outlet angle, α volute angle, α_d diffuser angle, g volute inlet gap, f inlet pipe fillet, p plate thickness

representation of pump-specific design parameters. Differently, in the present parametric Euler framework, each design dimension is separately represented, as in Eq. 1. Therefore, these parameters can be optimized for defined ranges based on predetermined hemodynamic or design targets, as the main prominent feature of the proposed model.

ΔP_{pump} is the pump head equal to the pressure difference between inlet and outlet compliance chambers where the pump is in silico implanted (in this study, LV and aorta compliance chambers, respectively). ΔP_{loss} stands for the pump losses including tubing, impeller and volute friction [26], diffuser friction and separation [27], blade loading [28],

$$\Delta P_{pump} = \rho w^2 r_2^2 - \rho w^2 r_1^2 - Q_{pump}\left(\frac{\rho w r_2}{tan\beta_2\left(2\pi r_2 b_2 - \left(t_{bl,2}/sin\beta_2\right)z_{bl}b_2\right)} - \frac{\rho w r_1}{tan\beta_1\left(2\pi r_1 b_1 - \left(t_{bl,1}/sin\beta_1\right)z_{bl}b_1\right)}\right) - \Delta P_{loss} \quad (1)$$

wake region mixing [29], leakage between the rotation and

stationary parts [30], leakage from the blade pressure side to suction side [31], blade separation [32], blade incidence angle [33], and recirculation into the impeller [31]. Index *1* represents the inlet of the pump, while index *2* represents the outlet. Q_{pump} is the pump flow rate and w is the rotational speed. Other impeller and blade design parameters which are not represented in the governing equation explicitly but have a role in the loss calculations are shown in Fig. 1 on the baseline FDA pump drawings.

FDA Pump System-Level Design Optimization

Circulation system-level (LPM) design optimization has been conducted with an in-house developed tool, which searches the global optimal values of design parameters based on specified objective functions. Except $r_{d,i}$, which is determined indirectly using the other parameters, and f and g, which are held constant in this study, all design parameters represented in Fig. 1 are included in the optimization procedure. For this aim, each design parameter was changed within a range around the baseline FDA pump values, one at a time to observe their effects on changes in the normalized objective function. In this study, the objective function $f_N(x)$ for a target optimal pump is constructed as a composition of healthy cardiac output (CO) and aortic pressure with blade tip velocity, and as another optimization case, blood-wetted area of the device, as these are among the indicators of hemolysis, thrombogenicity, and hemocompatibility [34, 35]. Equation 2 quantifies deviations from target hemodynamic values under both healthy and LV failure (LVF) conditions without pump support, ensuring robust LVAD performance across physiological states. To balance variables with different scales, the function uses normalization based on nadir (worst acceptable) and utopia (ideal) values. This prevents any one metric from dominating the optimization. Such multi-objective normalization is standard in global optimization, supporting designs that meet diverse physiological requirements.

$$f_N(x) = \sum_{i=1}^{N} (we_i)\left(\frac{X_{i,healthy} - X_i(\bar{x})}{X_{i,healthy} - X_{i,LVF}}\right) \tag{2}$$

where X_i represents the objective parameters of the optimization and $i = 1 \ldots N$ where N is the number of objectives that constitute the composite objective function. Subscripts *LVF, FDA*, and *healthy* represent the value of associated objective in LV failure, FDA pump operation, and healthy circulation states, respectively. $X_i(\bar{x})$ defines the relevant objective's value for a set of pump design parameters $\bar{x}$. *we* is the weighting factor corresponding to each individual objective and the sum of all weights equals to one. Finally, $\bar{x}$ is the set of pump design parameters to be optimized.

A genetic algorithm is used for the optimization of $f_N(x)$. Optimization algorithm initializes with a population of design parameter sets and evolves them through selection, crossover, and mutation, evaluating each using the $f_N(x)$, while different pump designs are iterated until the change in $f_N(x)$ of the recent pump is smaller than the convergence criteria ε_1 (Optimization Algorithm). Similar types of global optimization algorithms are widely used in the literature [6, 9], including in our own earlier works [36, 37]. For each pump design iterated during the optimization, an operation point is determined by revising the pressure of each compliant chamber under pump operation until the difference between the pump and system (LPM) pressures is smaller than a convergence criterion ε_2 (Physiology Match Constraints). These pump–physiology match and pump optimization algorithms are shown in Fig. 1.

Volute is designed after the determination of main dimensions via optimization by assuming the pressure and the average velocity in volute to be nearly constant. Once the optimal design parameter set is found, volute is divided into several cross-sections. Average velocity at each cross-section is set to be the same as the diffuser inlet velocity

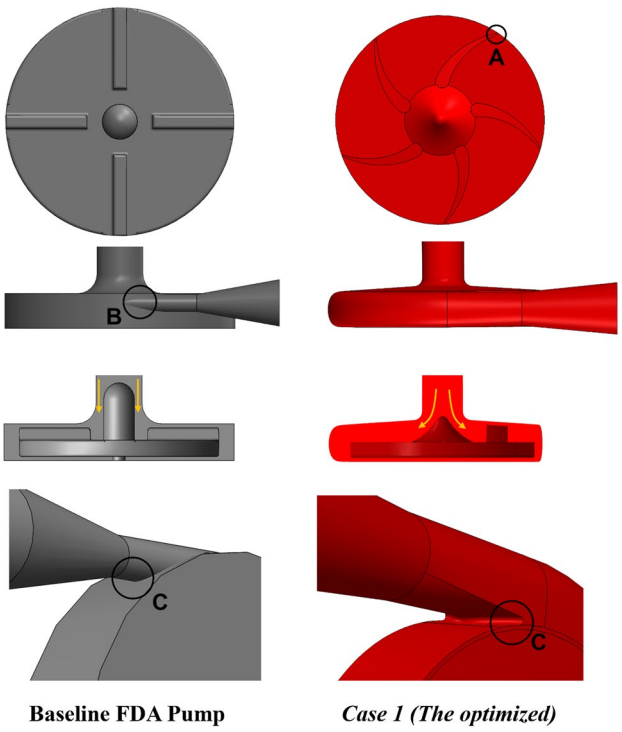


Fig. 2 3D design comparison of baseline FDA pump (*left*) vs. optimization *Case 1 (right). Detail A* represents the changed blade shape, *detail B* highlights the change in diffuser connection to volute, *yellow*-colored arrows represent the adapted inlet guide vane and hub design of the optimized model, and *detail C* compares the smooth volute tongue design of the optimized pump with the baseline FDA pump

calculated through Q_{pump} and $r_{d,o}$, based on the Stepanoff method assuming the cross-sections are circular [38]. Thus, this approach for volute optimization is uncoupled from the pump optimization, but other "coupled" volute design approaches can easily be implemented in this scheme.

Detailed Design Considerations CAD (LPM to 3D CAD Model)

Inlet dome design: Keeping the average velocity constant as much as possible from the pump inlet to the blade passage is crucial for hydrodynamic performance and reduced hemolysis. Thus, a proper inlet guide passage is designed with a dome in the middle of impeller, creating a conical area between impeller and shroud. This conical flow area is controlled through tuning parameters f and r_1 to keep it constant plus to ensure constant average blood velocity. The comparison of flow fields through the improved inlet guide passage with the baseline FDA design inlet is shown in Fig. 2. For an unbiased comparison, the leakage gap between the blade upper surface and shroud is kept at 1 mm in all optimized pumps as in the baseline FDA design. Likewise the impeller plate height is kept same (4 mm).

Volute cross-section design: The volute inlet cross-section was designed as trapezoidal, and the other volute cross-sections are designed using Bezier curves. Thus, once the volute cross-sectional areas are computed via Stepanoff method, each section of volute is transformed into the Bezier curves defining smooth transition with the shroud and hub and preserving the computed hydraulic area. For this optimization, the trapezoidal cross-section at the volute inlet, a gap of 0.5 mm (parameter g in Fig. 1) is set as constant for all designed pumps for simplicity, which can also be varied in the optimization if needed. Importantly, these Bezier curves at each cross-section is constructed preserving the taper angle of blades to minimize wake regions at impeller to volute flows.

While designing the volute, these Bezier curves were transformed into the points (coordinates) from LPM to a computer aided design (CAD) system, for each cross-section at each angle of volute, and connected via Bezier curves at each cross-section. Designing the volute in CAD by generating the Beziers at each angle of volute is laborious. Thus, we compared the volute profile obtained via cross-sections at each 10 degrees of volute with the following cases in Geomagic software: (a) cross-sections at each 30 degrees of volute, (b) cross-sections at each 20 degrees of volute, and (c) a refined one to the inlet and outlet of volute from 20 degrees to 5 degrees. As demonstrated in Fig. 3, the refined profile yields a very similar shape with the design having a cross-section at each 10 degrees. Thus, such refined design method was used in this study for the volute generation.

Blade shape: Optimization tool provides only the optimal dimensions for design parameters listed in Fig. 1; thus, there is a further step required to determine whole blade shape and curvature. For this aim, the blade to be generated is divided into segments, and Eq. 1 is solved to obtain inlet and outlet angle of each blade segment. ΔP_{pump} is initially assumed as distributed to the segments equally, but updated by simultaneously solving the Euler turbomachinery equation for each segment through an implicit solver until convergence is achieved across all segments, and the constant Q_{pump} is used for each blade segment. Once the inlet and outlet angles are calculated for each segment, segment chords are drawn using the average of inlet and outlet angles. As the final step, blade curvature is generated by the connecting segment chords from pump inlet to outlet. The blade thickness is reduced equally from both the suction and pressure sides along the chord, reaching ~ 0.3 mm at the blade outlet tip, as seen in *detail A* at the top of Fig. 2. Blade inlet curvature is circular with its diameter equal to blade thickness.

Volute tongue and diffuser: Different than the baseline FDA, the volute tongue is also designed to be smoother using a fillet, as seen in the *details C* at the bottom of Fig. 2. The volute spiral was constructed in SolidWorks using Bezier curves based on coordinates from the design framework. A loft operation connected the spiral outlet to the diffuser inlet, forming the volute tongue. A fillet with a ranging radius between 0.5 and 1 mm ensures a smooth transition to the circular diffuser, which was completed by lofting between its inlet and outlet. It also shows that the Bezier curve at the volute outlet is softly connected with the diffuser inlet using a loft preserving the cross-sectional area constant and ensuring the absolute velocity outflow vector is perpendicular to these cross-sections. As another remark, diffuser collects all the flow at the volute outlet to minimize the losses different than the baseline design in which the diffuser is located at a portion of volute outlet, as seen in the second row of Fig. 2 (detail B).

Computational Fluid Dynamics (CFD)

To verify the LPM predictions, we developed a CFD model in OpenFoam and validated it rigorously against experimental data from the literature [23], as well as our own PIV experiments [39]. The Multiple Reference Frame (MRF) method is utilized to handle the rotating frame. The simpleFoam solver in OpenFOAM [40] was employed, utilizing a steady-state solver with the SIMPLE pressure–velocity coupling algorithm. Second-order spatial discretization was applied for improved accuracy. Menter's $k-\omega-SST$ [41] model was selected for RANS turbulence modeling, since this model provides reliable results in adverse pressure gradients that would be critical to assess separation cases. We have ensured that the first cell height provides

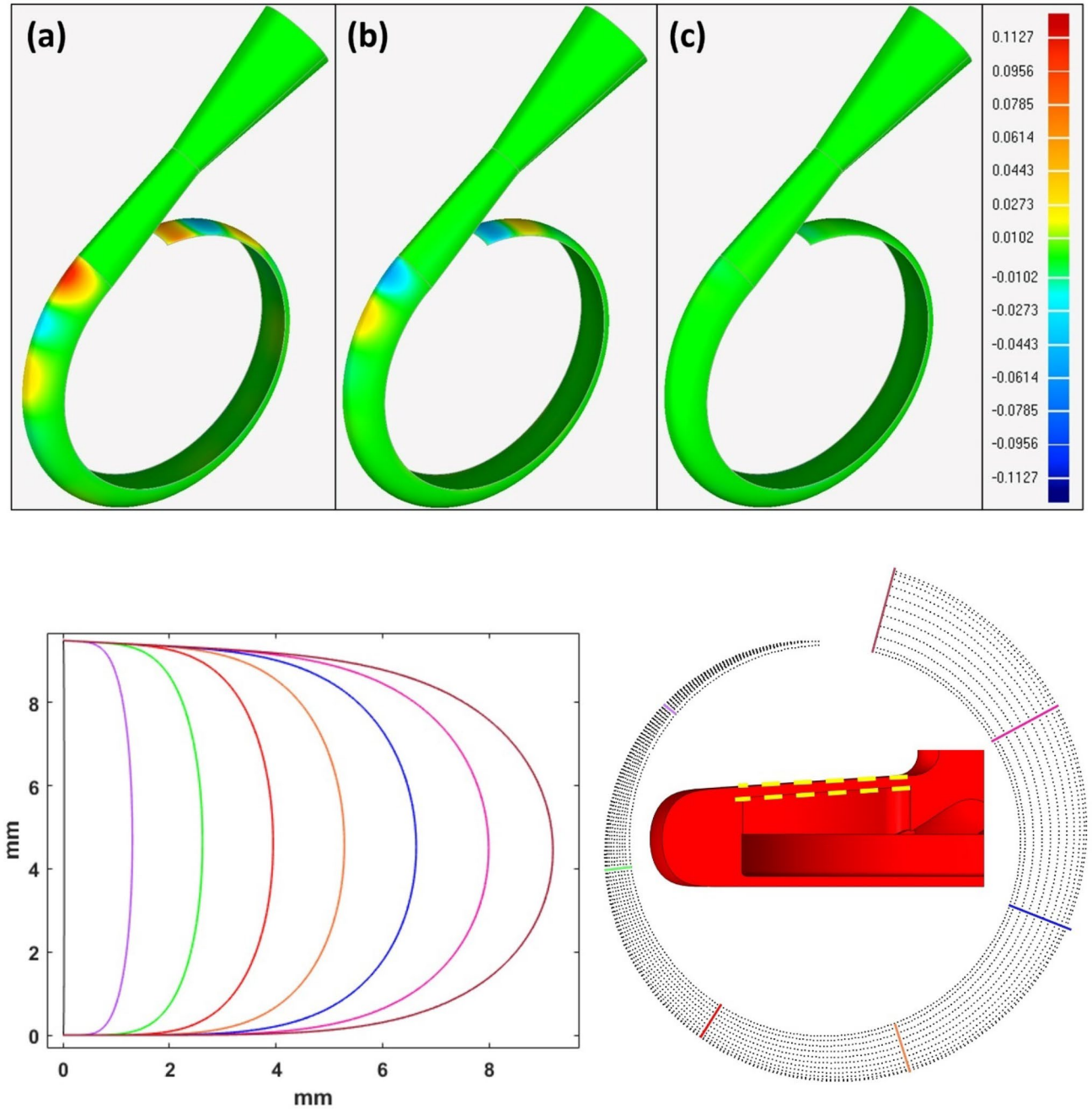


Fig. 3 **a** Volute profile differences (in mm) of cross-sections at each 30 degrees vs. 10 degrees. **b** Volute profile differences (in mm) of cross-sections at each 30 degrees vs. 20 degrees. **c** Volute profile differences (in mm) of cross-sections refined at inlet and outlet vs. at each 10 degrees. ***Bottom***: Coordinate points transferred from LPM to CAD, and Bezier curves represented via different colors for sample cross-sections. A section view was shown in the middle to present the tangency of top and bottom of shroud to the volute cross-section Beziers

low y^+ distribution in all solid surfaces. In all numerical simulations, the y^+ plus remained below unity on all surfaces assigned to no-slip wall boundary conditions, while the maximum y^+ was less than 3. Therefore, we have maintained first cell calculations in the laminar sub layer.

A grid consisting of hexahedral boundary layer elements and tetrahedral core elements was generated for the numerical simulations. To ensure grid independence, three grid configurations were tested, with cell counts doubled (2.5, 5, and 10 M cells), and the pressure head created by the pump was monitored. With a difference less than 2% between the

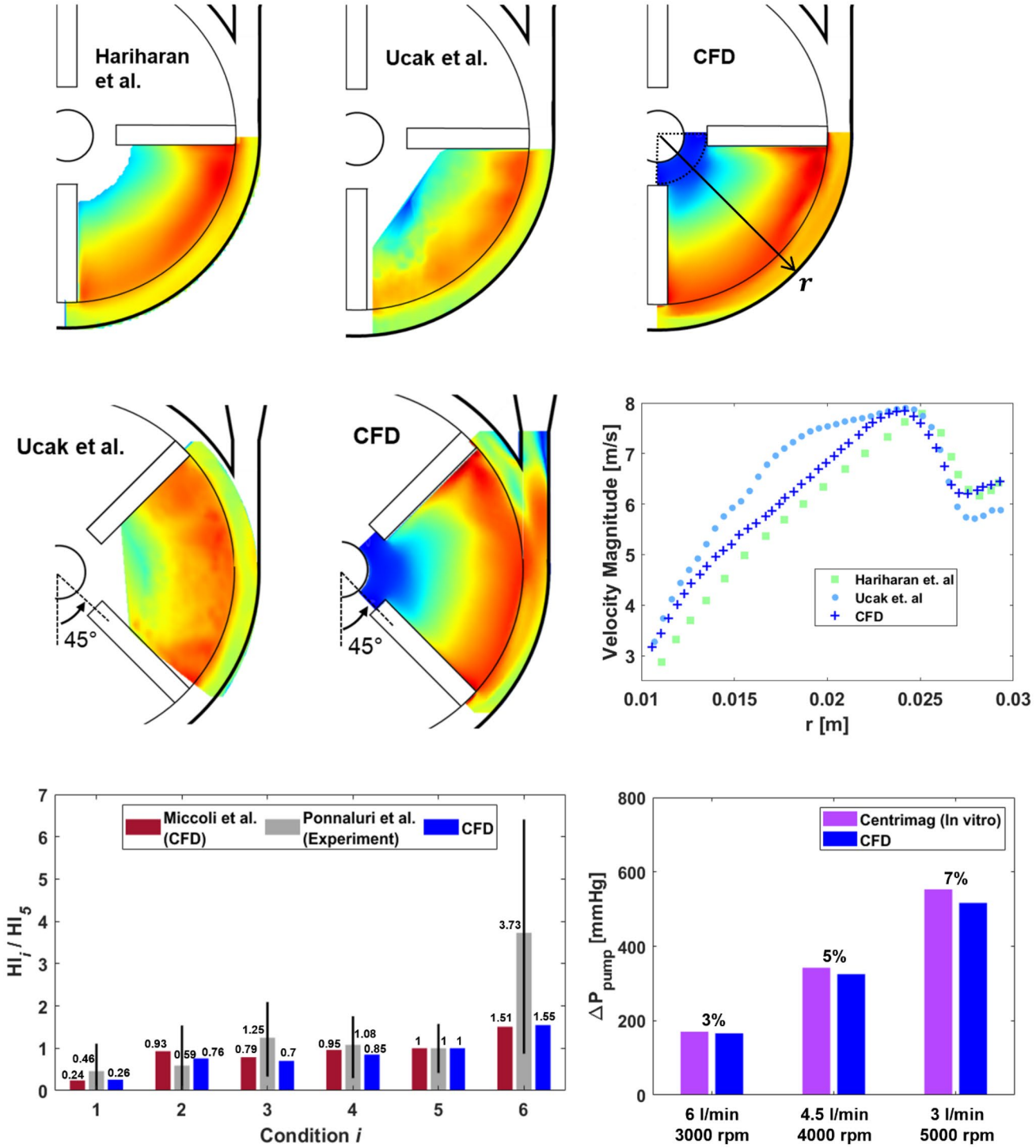


Fig. 4 *Top*: Orientation-based velocity field and mean velocity magnitude along with the given line of the blade passage region (represented by *r*) comparisons for *Condition 2*. ***Bottom***: Comparison of our CFD-simulated hemolysis index (HI) with the Miccoli et al. [44] CFD results, and blood experiments (mean ± SD) conducted by Ponnaluri et al. [22], for the introduced conditions of FDA pump. HI values for all conditions are presented relative to *Condition 5*, which showed good agreement between the present model (5.34) and the reference CFD model [44] (5.14). Comparison of our CFD pressure results with the commercial Centrimag catalog data [45] under the introduced operation conditions

5 and 10 M grids, the 5 M grid was selected for further modeling.

Alongside solving the system of Reynolds-Averaged Navier–Stokes (RANS) equations, two additional scalar equations were solved to estimate the flow residence time (RT) [42] and the hemolysis index (HI) [43]. Both transport equations were implemented in OpenFOAM using the scalarTransport feature of the solver. In both equations, the diffusion constant was set to a very small value to omit the diffusion terms. For the RT equation, since the governing equations in simpleFoam are in non-conservative form and also divided by density, a unity source term was added. The HI model is based on a power-law approach with porcine blood constants and von Mises scalar stress. The validation of these models and the results obtained will be discussed next.

Figure 4 shows the validation of our CFD model from various perspectives. Mean velocity magnitudes plotted for the blade passage region were compared with the literature [23] and with our in vitro results [39], matching well. It also includes the validation of our CFD hemolysis model through the computational investigation results of Miccoli et al. [44] and blood experiments conducted by Ponnaluri et al. [22]. Additionally, the minimum RT, observed at the centerline having the highest velocity, was 0.10025 s, closely matching the analytical value of 0.1 s. We have validated the CFD model with another commercial pump Centrimag [45] as well, and the results yield an acceptable error up to ~ 9% compared to the VAD's catalog values of various operation conditions, as presented in Fig. 4. FDA pump simulations were also verified with the literature [23] and our previous in vitro research [39], both addressed alongside the LPM in the Results sections.

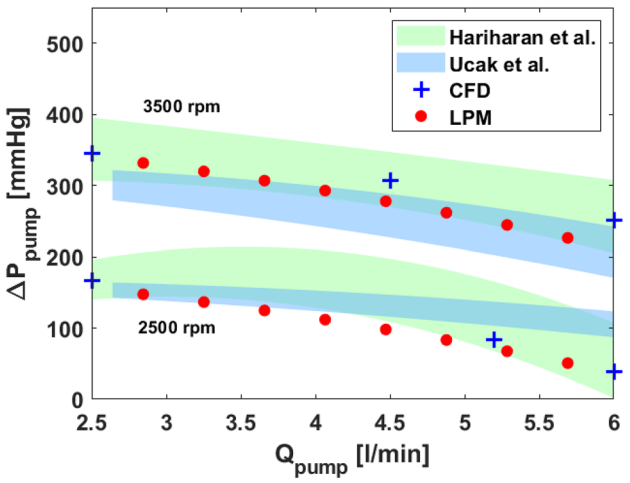


Fig. 5 Baseline FDA pump characteristic curves obtained for $w = 2500$ rpm and $w = 3500$ rpm. *Green*-shaded area represent the CFD and PIV result ranges obtained by Hariharan et al. [23] and *blue*-shaded area is the range obtained by our previous PIV study of Ucak. et al. [39] CFD simulations were conducted for *Condition 1* (2.5 l/min, 2500 rpm), *Condition 2* (2.5 l/min, 3500 rpm), *Condition 3* (4.5 l/min, 3500 rpm), *Condition 4* (5.2 l/min, 2500 rpm), *Condition 5* (6 l/min, 2500 rpm), and *Condition 6* (6 l/min, 3500 rpm) *Blue plus* signs represent our CFD results for the introduced conditions and *red circles* represent the LPM characteristic curves

Results

LPM Model Validation

For model validation, the computed baseline FDA pump characteristic curves via our LPM tool were compared with the literature [23], our previous in vitro research [39] and new CFD simulations conducted in this manuscript, as shown in Fig. 5. The CFD solver used for this task is experimentally validated as described earlier in the Methods section.

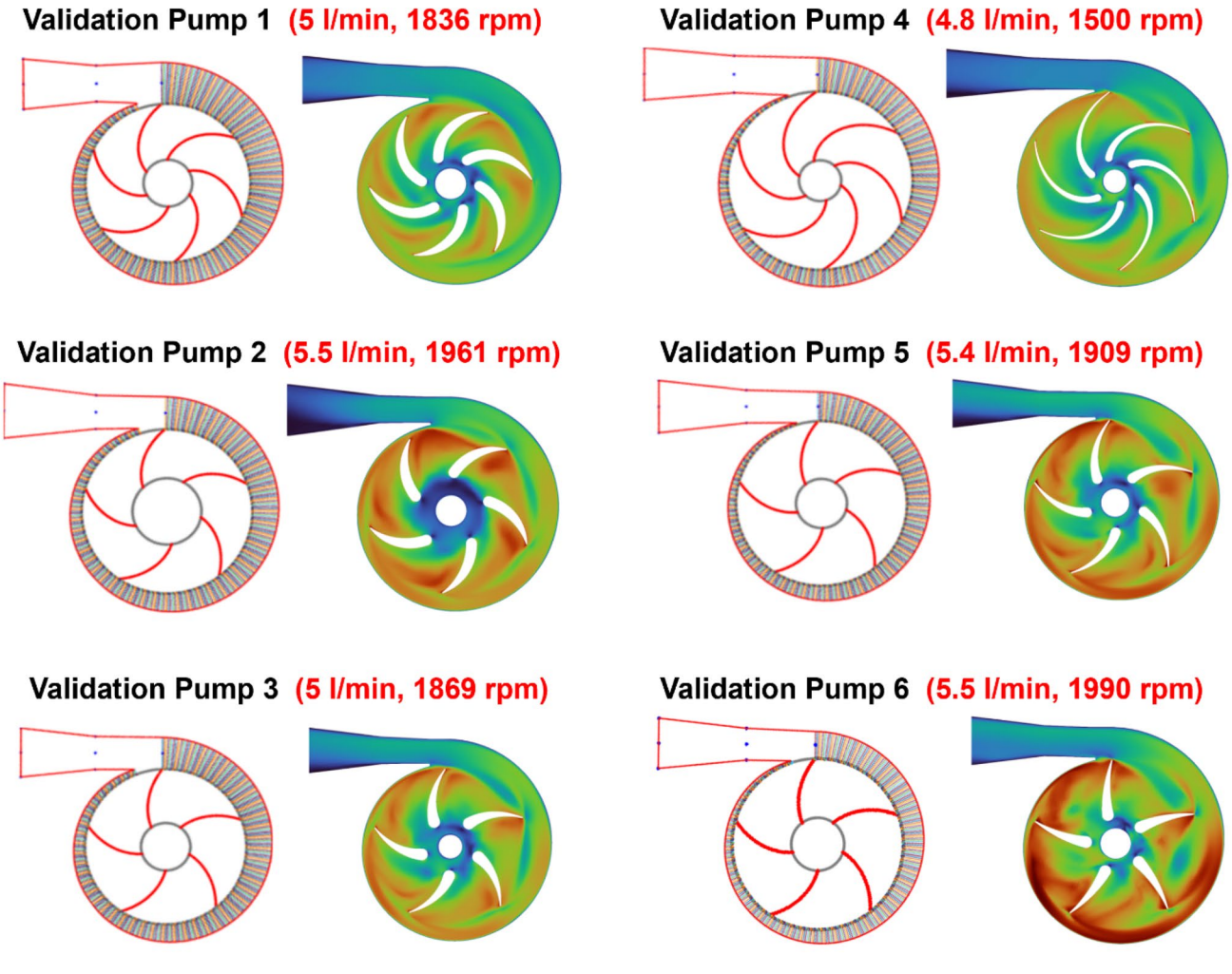
In addition to the above validation effort, we have selected 6 different blood pump geometries that are not optimized but analyzed via our LPM were compared with the CFD for further validation. Our results showed a discrepancy up to 12% at the design point, as given in Fig. 6 in detail. Additionally, a random pump chosen from the literature [46] and one of the most popular VADs, HeartMate III, were characterized through the proposed pump LPM model and compared with their *in vitro* measurements [47]. For these two available pumps in literature, LPM simulated the pump head at the design point with an error of 9% and 3%, respectively.

FDA Pump Optimization Cases

To illustrate our optimization approach, 7 different optimization cases were conducted. Among these cases, *Case 1* and *Case 5* are observed as the best designs in terms of reducing the blade tip velocity and blood-wetted area, respectively, by preserving the target hemodynamics CO and arterial pressure. Table 1 compares the key hemodynamics and characteristics of these optimized pump designs with the results obtained for healthy, acute LV failure, and the baseline FDA pump-implanted circulation states. This shows that the baseline FDA pump design can be improved by 32% in terms of reduced blade tip velocity and by 40% in terms of the reduced blood-wetted area through our optimization framework.

Effect of Design Parameter Space Used in Optimization

In addition, 7 different optimization cases were introduced based on the different bounds of sampling range for each design parameter in search space, different objective



	ΔP_{pump} (mmHg)		Error (%)
	LPM	CFD	
Validation Pump 1	71.24	65.42	**8.9**
Validation Pump 2	88.48	79.26	**11.6**
Validation Pump 3	73.81	69.95	**5.5**
Validation Pump 4	66.06	64.5	**2.4**
Validation Pump 5	85.43	81.00	**5.5**
Validation Pump 6	89.88	86.5	**3.9**

Fig. 6 Semi-arbitrary chosen pump cases for the validation of LPM with CFD simulations. All validation pumps were simulated at theird-esign operation conditions provided in parentheses their flow rate and rotational speed. In LPM 2D sketches, circle at the middle represents the inlet of the pump, yet, for CFD results it represents the 3D CAD converted hub, process described in the Methods Section. The inlet is the circular surface, not shown in these images, that connects the blade leading edges. ΔP_{pump} stands for the pump head

functions and different weights. Table 2 summarizes the captures and objectives of investigated cases, and Table 3 shows the optimized parameter set and chosen optimization search bound for each case. As introduced, *Cases 1*, *2*, *3,* and *4* have common objectives (targeting the lower blade tip velocity of pump), yet varying upper and lower optimization bounds. On the other hand, *Cases 5* and *6* were investigated

Table 1 Comparison of the key specifications of baseline FDA pump vs. optimization Case 1 and optimization Case 5

Hemodynamics	Healthy	Acute LV failure	Baseline FDA pump	Case 1	Case 5
Aortic pressure (mmHg)	119/63 (92)	88/47 (67)	92	92	92
LV EF (%)	60	30	n/a	n/a	n/a
RV EF (%)	56	44	56	56	57
CO (l/min)	5.2	3.75	5.26	5.2 l/min	5.2
Rotational speed (rpm)	n/a	n/a	2410	1876	2317
Pump pressure (mmHg)	n/a	n/a	81	82	82
Pump flow (l/min)	n/a	n/a	5.26	5.2	5.2
Blade tip speed (m/s)	n/a	n/a	**6.82**	**4.64**	**5.23**
Blood-wetted area (m^2)	n/a	n/a	**0.0143**	**0.0107**	**0.0085**

Table 2 Optimized tip velocity and blood-wetted area of each case is presented

Case set 1	Objective set 1	Optimization search range	Tip velocity (m/s)	Wetted area (m^2)
Case 1	1. Cardiac output of 5.2 l/min ($we = 0.4$) 2. Mean aortic pressure of 92 mmHg ($we = 0.4$) 3. Minimum blade tip velocity ($we = 0.2$)	Baseline bounds	**4.64**	0.011
Case 2		LB and UB of w are changed	**3.87**	0.0135
Case 3		LB and UB of β_1 and β_2 are changed	**4.83**	0.01
Case 4		LB and UB of r_1 are changed	**4.8**	0.011
Case set 2	Objective set 2	Optimization search range	Tip velocity (m/s)	Wetted area (m^2)
Case 5	1. Cardiac output of 5.2 l/min ($we = 0.4$) 2. Mean aortic pressure of 92 mmHg ($we = 0.4$) 3. Minimum blood-wetted area ($we = 0.2$)	Baseline bounds	5.23	**0.0085**
Case 6	1. CO of 5.2 l/min ($we = 0.2$) 2. Mean aortic pressure of 92 mmHg ($we = 0.2$) 3. Minimum blood-wetted area ($we = 0.6$)		4.88	**0.0085**
Case 7		LB and UB of all design parameters are changed	5.41	**0.0055**
FDA pump	n/a	n/a	6.825	0.0143

The baseline parameter ranges and corresponding changes for each case are given in Table 3 in detail

LB lower bound, *UB* upper bound, *we* weighting factor of each individual objective, generating the objective function

for another objective set (targeting the minimum blood-wetted area of pump), although they were within the same optimization search area as *Case 1*. As a final case, *Case 7*, same objective of minimum blood wetted area was analyzed with a slightly-altered range for each parameter.

Although we have two different optimized pumps for two main objective functions of reduced blade tip velocity (*Case 1*) and reduced wetted area (*Case 5*), *Case 1* was chosen as the principal optimization geometry for the further hydrodynamic and hemolysis investigations via CFD. Thus, Fig. 2 shows the detailed 3D demonstration of impeller, blade and volute of *Case 1* comparatively with the baseline FDA pump design components.

The provided design tool can simply sketch the generated pumps in two dimensions (2D) for rapid visualization of the generated optimized shape subject to the detailed design considerations explained in "Detailed Design Considerations CAD (LPM to 3D CAD Model)" section. Therefore, the 2D sketches of all examined cases are demonstrated in Fig. 7 for a preliminary insight before the detailed 3D design.

Investigation of Detailed Flow Pathways via CFD: Baseline FDA Pump vs. the Optimized Designs

A numerical model has been created for both baseline FDA and the optimized case (*Optimization Case 1*). Figure 8 presents the comparison of velocity, RT, and HI CFD contours for both FDA pump and optimized case.

This figure shows that the volume of the optimized pump has reduced by about 48% (40.9 cubic centimeters for optimized vs. 78.3 cubic centimeters for baseline FDA pump), due to overall reduced dimensions in the optimized design. Furthermore, lower rotational speed (1876 RPM vs. 2500 RPM) in the optimized design has led to reduced

Table 3 The optimized values and the initial optimization search bounds of each design parameter used in pump optimization cases

Parameter	FDA	Case 1	Case 2	Case 3	Case 4	Case 5	Case 6	Case 7
$r_1(mm)$	7.5	5–8.5 (7.3)	5–8.5 (7.1)	5–8.5 (7.9)	**7.5-12 (10.3)**	5-8.5 (7)	5-8.5 (8.1)	**3.8-6 (5.4)**
$r_2(mm)$	26	20–26 (23.6)	20–26 (25.6)	20–26 (22.1)	20-26 (24.1)	20-26 (21.5)	20-26 (21.4)	**15-20 (16.6)**
$t_{bl}(mm)$	3	2–4 (3.1)	2–4 (2.7)	2–4 (2.8)	2-4 (3.1)	2-4 (2.7)	2-4 (3)	**1-2 (1.5)**
$z_{bl}(-)$	4	4–6 (5)	4–6 (5)	4–6 (5)	4-6 (5)	4-6 (4)	4-6 (4)	**4-6 (4)**
$w(rpm)$	2500	900–2500 (1876)	**900–1500 (1438)**	900–2500 (2078)	900-2500 (1900)	900-2500 (2317)	900-2500 (2169)	**1200-3200 (3104)**
$r_{d,i}(mm)$	2.2	4.4	5.8	4.1	4.8	3.3	3.8	**3.7**
$r_{d,o}(mm)$	6	4–8 (6.9)	4–8 (7.6)	4–8 (6.7)	4-8 (7.6)	4-8 (6.6)	4-8 (6.3)	**3-6 (5.4)**
$l_d(mm)$	21.54	16–30 (24.2)	16–30 (19.9)	16–30 (26.1)	16-30 (24.2)	16-30 (27.5)	16-30 (19.8)	**12-22.5 (14.9)**
$\alpha_d(deg)$	10	5–8 (5.97)	5–8 (5.3)	5–8 (5.65)	5-8 (6.6)	5-8 (6.9)	5-8 (7)	**5-8 (6.5)**
$l_t(mm)$	20	15–25 (18.9)	15–25 (19.3)	15–25 (19.7)	15-25 (17.8)	15-25 (20)	15-25 (18.1)	**11.3-18.8 (14.3)**
$b_1(mm)$	3	2.5–5 (4.7)	2.5–5 (5)	2.5–5 (4.5)	2.5-5 (4.8)	2.5-5 (4.7)	2.5-5 (4.1)	**1.8-3.8 (3.1)**
$b_2(mm)$	3	2.5–5 (3.6)	2.5–5 (4.8)	2.5–5 (3.6)	2.5-5 (3)	2.5-5 (3.2)	2.5-5 (3.8)	**1.8-3.8 (2.9)**
$\beta_1(deg)$	90	10–90 (64)	10–45 (62)	**10–45 (39)**	10-90 (61)	10-90 (65)	10-90 (65)	**10-90 (66)**
$\beta_2(deg)$	90	10–90 (53)	10–45 (33)	**10–45 (34)**	10-90 (55)	10-90 (66)	10-90 (81)	**10-90 (62)**
$\alpha(deg)$	30	10–25 (16)	10–25 (17)	10–25 (17)	10-25 (19)	10-25 (17)	10-25 (20)	**10-25 (20)**

$r_{d,i}$ is not obtained via optimization, it is indirectly calculated using the optimized values of $r_{d,o}$ and l_d

r_1 impeller inlet radius, r_2 impeller outlet radius, t_{bl} blade thickness, z_{bl} blade number, $r_{d,i}$ diffuser inlet radius, $r_{d,o}$ diffuser outlet radius, l_d diffuser length, l_t throat length, b_1 blade inlet width, b_2 blade outlet width, b_3 volute width, β_1 blade inlet angle, β_2 blade outlet angle, α volute angle, α_d diffuser angle

Each parameter with modified lower and upper bounds for the relevant case is highlighted in bold

velocity in the pump. The reduced dimensions combined with the reduced rotational speed reduce the tip speed. This leads to reduced stress exerted on the blood elements flowing through the pump. For instance, the peak velocity in the mid-blade plane for the baseline pump is about 8.1 m/s, while with a reduction of 41%, this value is about 4.8 m/s in the optimized pump. On the other hand, despite reduced speeds in the optimized pump, the volumetric average of the residence time has decreased in this (0.288 vs. 0.522 s, 45% decrease). This suggests reduced local flow entrapments within the device and the optimization process has improved washout characteristics. The optimized pump potentially minimizes the risk of thrombus formation by enhancing flow-through efficiency. Finally, the HI has drastically decreased in the optimized design, as seen in Fig. 8. While the mass-weighted average of HI at the outlet is ~ 3.55 for the baseline FDA pump, this value reduces to about ~ 0.4 in the optimized design (leading a 89% reduction).

Discussion

Optimization of blood-wetted devices traditionally focused on component-level (3D) or detailed shape optimization studies primarily using CFD or structural solvers, e.g., inlet and outlet canula optimization of VADs [48] or coronary artery stent shapes to achieve atheroprotective wall shear stress patterns [49]. In this traditional approach, the hemodynamic requirements such as blood flow rate and pressure drops are fixed as boundary conditions and were treated to be independent of the device geometric parameters. However, there is no guarantee for the optimized device component to work exactly at these fixed flowrate and pressure values when implanted to the actual patient. Thus, as an important progress, the present approach eliminated this problem by including the physiological parameters into the optimization loop allowing realistic device-vascular coupling. Most importantly, this feature allows the introduction of special *"physiological objective functions"* where chronic vascular adaptations and remodeling that occur following device implantation can also be modeled in a fully coupled way to the device geometry and other device design parameters.

In this study, FDA centrifugal blood pump is aimed to be optimized to provide healthy level of CO (5.2 l/min) and mean aortic pressure (92 mmHg) with lower blade tip velocity (constituting the *Objective Set 1*) and blood-wetted area (constituting *the Objective Set 2*), as an indicator of lower blood damage. Seven different optimization cases via changing bounds of design parameters and objective functions were also conducted as introduced in Tables 2 and 3. Table 1 shows that the target healthy CO and mean aortic pressure were reached with optimization

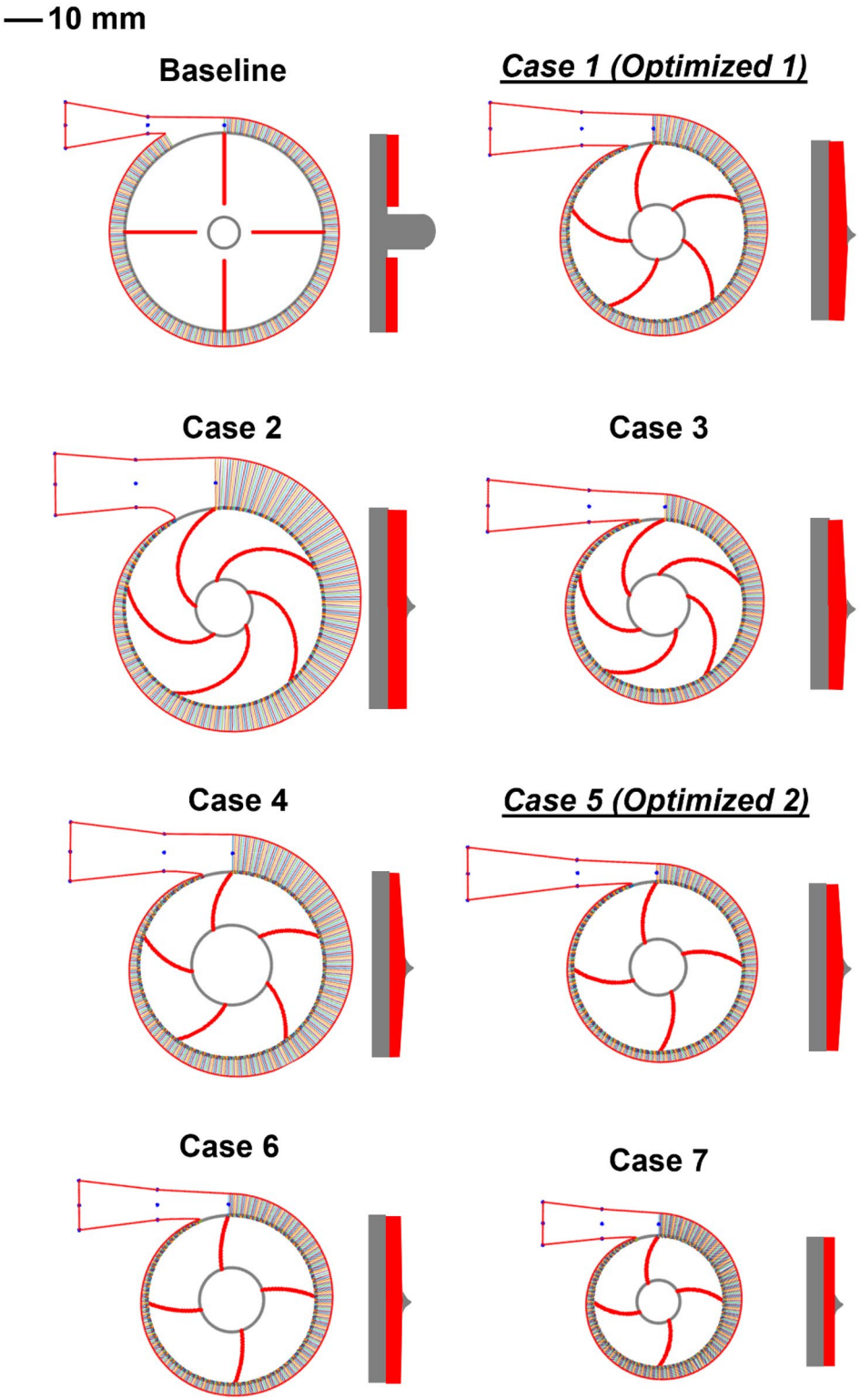


Fig. 7 2D sketches, top and side views, of all introduced optimization cases and the baseline FDA pump design

Case 1 pump with 32% lower rotational speed than the baseline FDA pump. Convergence of the normalized objective function in optimization *Case 1* through generations is plotted in the Supplementary Information. Alternatively, *Case 5*, another optimal case determined for the objective function of blood-wetted area showed that the same healthy level hemodynamics with the baseline FDA pump can be reached with an optimized pump having even a smaller blood-wetted area of 40%. Overall, these are amazing performance improvements that would be very

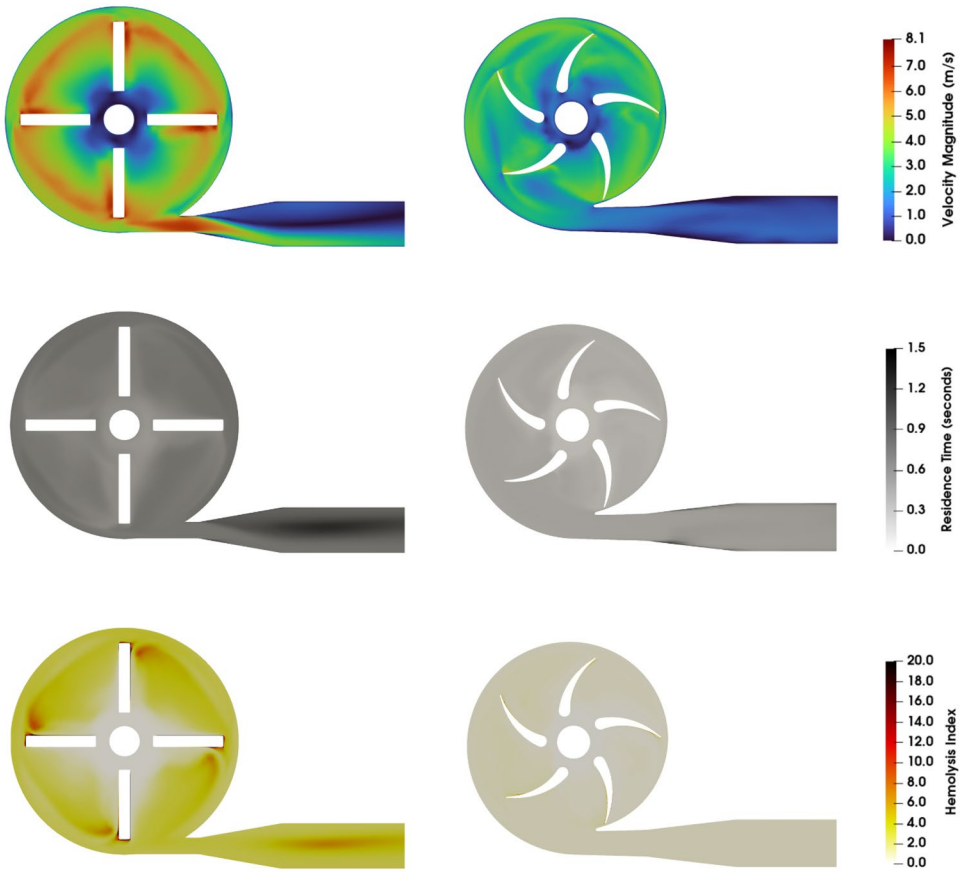


Fig. 8 Baseline FDA pump vs. the *optimization case 1* comparison of velocity magnitudes (*top row*), volumetric averaged residence time (*middle row*) and hemolysis index (*bottom row*)

difficult to be discovered without the present optimization framework.

To understand and quantify the influence of design parameters' on the reduced blade tip velocity objective, a detailed parametric sensitivity study was conducted. Effects of selected design parameters are plotted and summarized via a Pareto chart displayed in Supplementary Information. It demonstrated that the chosen objective function is most sensitive to r_2 and w, as expected due to their direct effect on tip velocity. Secondary to these, key parameters, b_1, b_2 and z_p were also identified to have significant effect on the objective function among the other pump dimensions. Sensitivity study also showed that diffuser and volute design parameters have relatively less effective compared to the impeller parameters on the objective function. Intrinsically, design parameter sensitivities differ for each objective, and it is important to determine optimization search bounds for each constructed objective function. While not considered in this initial work, our tool also enables us to formulate a wide range of hemodynamic and cardiovascular design objective functions, such as lower blood-wetted area to reduce thrombogenicity, target ventricular EF values or pressure–volume curve shapes, end-organ hemodynamic targets like pulmonary-to-systemic flow ratio, cerebral and coronary flow, hepatic/renal conditions, and oxygen saturation levels. Furthermore, our model can optimize blood pumps for operation under any desired exercise condition of the patient [50].

As further discussions on *Objective Set 1* cases (Table 3), modifications in range of w revealed that impeller outlet radius and rotational speed are inversely changed through the optimization as expected (*Case 2*). In *Case 3*, reduced blade inlet and outlet angles increase the mean blade length and consequently blade loading and recirculation losses. These losses were compensated by selecting a smaller radii/larger length diffuser and increasing the rotational speed. On the other hand, *Case 4* can operate lower speeds than the other cases due to its smaller impeller inlet radius, which also causes a lower radial velocity at the pump inlet. In this case, impeller outlet blade width was decreased to create a corresponding reduction in the outlet radial velocity to maintain the target aortic pressure and CO.

Considering *Objective Set 2*, main contributors to the pump blood-wetted area are determined to be the impeller top and bottom surfaces, followed by the shroud inner surface, and finally the volute inner surface. In *Cases 5* and *6*, impeller surface area was slightly decreased, yet, it does not significantly contribute to the reduction of blood-wetted area due to the same search range bounds of these design

parameters with *Case 1*. Therefore, the algorithm used an alternative way to minimize the wetted area, by reducing the inner surface of Bezier cross-sections in volute via reducing the diffuser inlet and outlet radii (Table 3). Due to the constant average velocity assumption used in this study, volute shape can be indirectly manipulated through the diffuser design. The volute in the baseline pump has a constant radius and connects to the diffuser through a needle-shaped passage with a much smaller cross-sectional area compared to the volute. As seen in Fig. 8, this leads to a sudden acceleration of the flow in the baseline pump. This abrupt acceleration increases velocity gradients, which in turn elevate hemolysis. However, in the optimized pump, the volute has a spiral form designed to accommodate the accumulation of flow. Based on this design, no sudden changes in flow speed are visible within the volute, as shown in Fig. 8. Additionally, this figure illustrates that the smooth integration of volute and diffuser ensures a smooth flow transition between these two regions. Finally, in *Case 7*, the search bounds for all parameters were adjusted to a lower range to observe the broader impact of these ranges on the objective function. As foreseen, it generated the smallest case design with an extreme reduction in the blood-wetted area of 61% than the FDA pump, but with the highest rotational speed to achieve the target hemodynamics. Reduced blood-wetted area or device volume is a widely desired clinical need in neonatal and pediatric mechanical support applications, not only for achieving compact devices but to eliminate neonatal blood reactivity issues.

The LPM-Euler turbomachinery formulation employed in this study is based on a major assumption where relative flow pathways are considered parallel to the device blade surfaces. Thus, this formulation will predict the performance at the design operating conditions with the best accuracy, with an error of 2.5%. However, we observed that due to our detailed loss prediction modules, we were also able to predict the off-design operating points acceptably well with a maximum error of 15%, despite the lack of an operable design point in FDA pump due to the straight blades. As an example, baseline FDA pump curves simulated via our model for rotational speeds of 2500 and 3500 rpm were compared with the literature, as seen in Fig. 5. It shows that both LPM and CFD results have a good agreement with the literature ranges given by Hariharan et al. [23]. The differences observed between our LPM and CFD results for the introduced conditions can be summarized as follows: 6% in *Condition 1* (2.5 l/min, 2500 rpm), 1% in *Condition 2* (2.5 l/min, 3500 rpm), 9% in *Condition 3* (4.5 l/min, 3500 rpm), 14% in *Condition 4* (5.2 l/min, 2500 rpm), 2% in *Condition 5* (6 l/min, 2500 rpm), and 15% in *Condition 6* (6 l/min, 3500 rpm). The mean absolute error across all conditions was ± 8% at off-design operating points. As expected, the deviation between LPM and CFD slightly increases at the off-design regions from the design operating point, due to empirical errors in loss formulations. Nevertheless, both LPM and CFD results are observed in the range of our previous PIV research on FDA pump [39] and literature [23]. Additionally, Fig. 3 demonstrates that the velocity magnitude along radial line of the blade passage and blade orientation-based velocity fields obtained through CFD for the baseline FDA pump at *Condition 2* matched well with the in vitro studies. This figure also demonstrates that the simulated HI for all introduced FDA pump conditions are consistent with literature-based CFD studies and fall within the standard deviation range observed in porcine blood experiment measurements.

Figure 4 also presents the further validation of our CFD model with literature numerical [44] and experimental data [23]. The figure demonstrates that the relative HI varies significantly with operating conditions, even when the design remains the same. Additionally, the absolute HI values were observed to be 1.39, 4.06, 3.74, 4.54, 5.34, and 8.28 for *Conditions 1* through *6*, respectively, further revealing the substantial impact of operating conditions on HI. A similar study was conducted for the *Case 1* design using *Condition 5* from Hariharan et al. [23] as the reference. It was observed that the absolute HI is 83% lower at the design condition compared to its operation under *Condition 5*.

CFD results presented in Fig. 8 show the evident of various performance improvements at the component-level through optimization and detailed hydrodynamic design. The velocity contour plots revealed that the baseline pump exhibits regions of flow separation between blades and in the downstream of the diffuser. Additionally, a low velocity region is observed in the hub region of the impeller. In contrast, the optimized design displays a more uniform velocity distribution with minimized low-speed zones. The smoother transition of velocity magnitudes across the impeller and volute suggests improved flow streamlining in the pump, which contributes to improved hemodynamic performance.

Similarly, when the RT contours are investigated closely (Fig. 8), the baseline pump shows a region of locally elevated RT caused by flow separation in the diffuser downstream, which is completely diminished in the optimized design. Both pumps operate in the same flow rate. However, due to reduced volume, the optimized pump has a reduced flush time (volume divided by volumetric flow rate): 0.488 seconds for the optimized pump and 0.899 seconds for baseline (46% decrease).

Improvements in velocity and RT show their additive effect in the reduction of HI. The baseline pump exhibits elevated HI values near the leading edges of the impeller blades and at high-velocity gradient regions. This suggests that shear-induced hemolysis is a concern in the baseline design. In contrast, the optimized pump significantly reduces the peak HI values, particularly near the impeller blades. The

smoother transition in velocity and lower shear regions indicate that the optimized pump better mitigates RBC damage, leading to improved biocompatibility. Considering all these three variables investigated by CFD in detail, it is confirmed that the optimized design has considerably improved the performance via fulfilled optimization objectives.

The performance of the optimized *Case 1* design was also compared with that of a clinically relevant pump, the CentriMag (Abbott, IL, USA), at operating conditions of 5.2 L/min and 82 mmHg. CentriMag is one of the clinically approved pumps with the lowest blood damage parameters. CFD simulations for both pumps showed that our *Case 1* design could deliver the same flowrate and pressure as the CentriMag, while operating at 11% lower rotational speeds. Additionally, similar blade tip speeds (~4.6 m/s) and hemolysis indices (~0.4) were observed under these common conditions. Notably, the optimized pump exhibited a residence time (RT) that was 3% shorter than that of the CentriMag. These findings indicate that even a benchmark pump such as the FDA design can be enhanced to reach the performance level a clinically approved device.

Although the optimization cases were conducted for full support of LV in this study, the proposed tool can investigate the partial support cases as well. However, it was observed that the LV in the selected failure state is unable to maintain adequate levels of CO and arterial pressure through partial support alone. A moderate acute LV failure state was used in this study, yet our model can analyze any severity of LV failure. Moreover, the proposed network has the flexibility to investigate any other congenital diseases or patient profiles via modifying the network.

As an additional consideration, applying the algorithm to mixed-flow or axial-flow pumps like the HeartMate III requires modifications to account for their 3D flow paths and velocity triangle geometry changes. Adaptation of the equations for such cases has already been initiated for our right ventricle assist device design research [51], and further development is ongoing.

Despite all these novelties it brings, the introduced model still has limitations. Firstly, since this is a 2-element LPM, the impedance factor in vessels is neglected. Secondly, while we demonstrated blood damage improvements using rigorously validated CFD results, further in vitro and blood tests are desired and ongoing through multiple optimized configurations. These will confirm a more robust hydrodynamic and hemolysis analysis framework. Finally, loss calculations, particularly friction factor estimation, might be improved via evaluation of the continuous test data to obtain a more accurate, comparable model with the CFD and *in vitro* studies even in off-design conditions.

In overall, considering all its flexibilities and advantages, this research has potential to contribute the mechanical circulatory support design process by serving primarily the preliminary design step, which may minimize the trial-and-error cycle at the detailed CFD design and experimental investigation phases. Conventional CFD-based, iteration-driven pump design and optimization can take several months. In contrast, the proposed framework delivers a comparable level of design insight within just a few days. Additionally, recent studies have shown a link between hydraulic dissipation and hemolysis [52, 53]. This would reduce the CFD analyses time significantly since HI calculations require an additional passive scalar equation to be solved numerically. Therefore, particularly for achieving the objective of truly customized patient-specific blood-wetted devices, this approach will comprehensively save time and prototyping resources significantly during the design process. As the first demonstration of this integrated design approach, the benchmark FDA blood pump has been significantly optimized with improved hydrodynamic profiles and hemocompatible detailed design features. This benchmark alternative is made openly available (https://doi.org/10.5281/zenodo.15076514) and can be considered especially in precise device development projects. This approach also allows us to consider new circulatory assist devices that are optimized for patient's specific physiology, which will be the focus of our future work.

Supplementary Information The online version contains supplementary material available at https://doi.org/10.1007/s10439-025-03834-8.

Author contributions CY and KP envisioned the study and developed the preliminary design tool framework. CY, KU, AM, and TG designed 3D models and conducted the computational work under the supervision of KP. HE primarily supervised the development of optimization-related tasks and ÖUB and KP primarily supervised the CFD studies performed by AM. All authors provided intellectual contribution, wrote and edited the manuscript text.

Funding This work was supported by the European Innovation Council (EIC) Transition Open Award*HeartWise101214454.*

Data Availability All data related to this project are maintained and curated by Pekkan Lab and Koc University Data Management infrastructure and available upon request.

Declarations

Conflict of interest The authors have no conflict of interest.

Open Access This article is licensed under a Creative Commons Attribution-NonCommercial-NoDerivatives 4.0 International License, which permits any non-commercial use, sharing, distribution and reproduction in any medium or format, as long as you give appropriate credit to the original author(s) and the source, provide a link to the Creative Commons licence, and indicate if you modified the licensed material. You do not have permission under this licence to share adapted material derived from this article or parts of it. The images or other third party material in this article are included in the article's Creative Commons licence, unless indicated otherwise in a credit line to the material. If

material is not included in the article's Creative Commons licence and your intended use is not permitted by statutory regulation or exceeds the permitted use, you will need to obtain permission directly from the copyright holder. To view a copy of this licence, visit http://creativecommons.org/licenses/by-nc-nd/4.0/.

References

1. Wiegmann, L., S. Boes, D. de Zelicourt, B. Thamsen, M. Schmid Daners, M. Meboldt, et al. Blood pump design variations and their influence on hydraulic performance and indicators of hemocompatibility. *Ann. Biomed. Eng.* 46(3):417–428, 2018. https://doi.org/10.1007/s10439-017-1951-0.
2. Li, Y., J. Yu, H. Wang, Y. Xi, X. Deng, Z. Chen, et al. Investigation of the influence of blade configuration on the hemodynamic performance and blood damage of the centrifugal blood pump. *Artif. Organs.* 46(9):1817–1832, 2022. https://doi.org/10.1111/aor.14265.
3. Wu, P., J. Huo, W. Dai, W. T. Wu, C. Yin, and S. Li. On the optimization of a centrifugal maglev blood pump through design variations. *Front. Physiol.* 12:699891, 2021. https://doi.org/10.3389/fphys.2021.699891.
4. Wu, J., B. E. Paden, H. S. Borovetz, and J. F. Antaki. Computational fluid dynamics analysis of blade tip clearances on hemodynamic performance and blood damage in a centrifugal ventricular assist device. *Artif. Organs.* 34(5):402–411, 2010. https://doi.org/10.1111/j.1525-1594.2009.00875.x.
5. Wu, J., J. F. Antaki, W. R. Wagner, T. A. Snyder, B. E. Paden, and H. S. Borovetz. Elimination of adverse leakage flow in a miniature pediatric centrifugal blood pump by computational fluid dynamics-based design optimization. *ASAIO J.* 51(5):636–643, 2005. https://doi.org/10.1097/01.mat.0000178966.79876.3d.
6. Ghadimi, B., A. Nejat, S. A. Nourbakhsh, and N. Naderi. Shape optimization of a centrifugal blood pump by coupling CFD with metamodel-assisted genetic algorithm. *J. Artif. Organs.* 22(1):29–36, 2019. https://doi.org/10.1007/s10047-018-1072-z.
7. Wang, C. N., F. C. Yang, V. T. T. Nguyen, and N. T. M. Vo. CFD analysis and optimum design for a centrifugal pump using an effectively artificial intelligent algorithm. *Micromachines*. 2022. https://doi.org/10.3390/mi13081208.
8. Liu, H., K. Wang, S. Yuan, M. Tan, Y. Wang, and L. Dong. Multicondition optimization and experimental measurements of a double-blade centrifugal pump impeller. *J. Fluids Eng.* 135(1):111031–1110313, 2013. https://doi.org/10.1115/1.4023077.
9. Torner, B., D. Frank, S. Grundmann, and F. H. Wurm. Flow simulation-based particle swarm optimization for developing improved hemolysis models. *Biomech. Model Mechanobiol.* 22(2):401–416, 2023. https://doi.org/10.1007/s10237-022-01653-7.
10. Escher, A., S. Miric, B. Thamsen, R. Giuffrida, P. Schmidt, B. Weinhold, et al. Multiobjective optimization of rotodynamic blood pumps: the use case of a cavopulmonary assist device. *ASAIO J.* 70(12):1074–1084, 2024. https://doi.org/10.1097/mat.0000000000002237.
11. Yazdanpanah-Ardakani, K., H. Niroomand-Oscuii, R. Sahebi-Kuzeh Kanan, and N. Shokri. Optimization of a centrifugal blood pump designed using an industrial method through experimental and numerical study. *Sci. Rep.* 14(1):7443, 2024. https://doi.org/10.1038/s41598-024-57019-9.
12. Yu-Qin, W., and D. Ze-Wen. Optimization design of hump phenomenon of low specific speed centrifugal pump based on CFD and orthogonal test. *Sci. Rep.* 12(1):12121, 2022. https://doi.org/10.1038/s41598-022-16430-w.
13. Hassan, A., A. Hashish, and S. Saleh. Simulation based design tool for radial impellers of centrifugal pumps. *Sci. Rep.* 14(1):13014, 2024. https://doi.org/10.1038/s41598-024-62808-3.
14. Pekkan, K., D. Frakes, D. De Zelicourt, C. W. Lucas, W. J. Parks, and A. P. Yoganathan. Coupling pediatric ventricle assist devices to the Fontan circulation: simulations with a lumped-parameter model. *ASAIO J.* 51(5):618–628, 2005. https://doi.org/10.1097/01.mat.0000176169.73987.0d.
15. Sisli, E., C. Yildirim, I. B. Aka, O. N. Tuncer, Y. Atay, M. Ozbaran, et al. Switching the left and the right hearts: a novel Biventricle mechanical support strategy with spared native single-ventricle. *Ann. Biomed. Eng.* 51(12):2853–2872, 2023. https://doi.org/10.1007/s10439-023-03348-1.
16. Di Molfetta, A., G. Ferrari, R. Iacobelli, L. Fresiello, M. Pilati, A. Toscano, et al. Acute biventricular interaction in pediatric patients implanted with continuous flow and pulsatile flow LVAD: a simulation study. *ASAIO J.* 62(5):591–599, 2016. https://doi.org/10.1097/MAT.0000000000000396.
17. Di Molfetta, A., A. Amodeo, L. Fresiello, M. G. Trivella, R. Iacobelli, M. Pilati, et al. Simulation of ventricular, cavo-pulmonary, and biventricular ventricular assist devices in failing fontan. *Artif. Organs.* 39(7):550–558, 2015. https://doi.org/10.1111/aor.12434.
18. V40 A. Assessing Credibility of Computational Modeling Through Verification and Validation: Application to Medical Devices. The American Society of Mechanical Engineers. 2018.
19. Malinauskas, R. A., P. Hariharan, S. W. Day, L. H. Herbertson, M. Buesen, U. Steinseifer, et al. FDA benchmark medical device flow models for CFD validation. *ASAIO J.* 63(2):150–160, 2017. https://doi.org/10.1097/MAT.0000000000000499.
20. Avci, M., M. Heck, E. A. O'Rear, and D. V. Papavassiliou. Hemolysis estimation in turbulent flow for the FDA critical path initiative centrifugal blood pump. *Biomech. Model. Mechanobiol.* 20(5):1709–1722, 2021. https://doi.org/10.1007/s10237-021-01471-3.
21. Heck, M. L., A. Yen, T. A. Snyder, E. A. O'Rear, and D. V. Papavassiliou. Flow-field simulations and hemolysis estimates for the food and drug administration critical path initiative centrifugal blood pump. *Artif. Organs.* 41(10):E129–E140, 2017. https://doi.org/10.1111/aor.12837.
22. Ponnaluri, S. V., P. Hariharan, L. H. Herbertson, K. B. Manning, R. A. Malinauskas, and B. A. Craven. Results of the interlaboratory computational fluid dynamics study of the FDA benchmark blood pump. *Ann. Biomed. Eng.* 51(1):253–269, 2023. https://doi.org/10.1007/s10439-022-03105-w.
23. Hariharan, P., K. I. Aycock, M. Buesen, S. W. Day, B. C. Good, L. H. Herbertson, et al. Inter-laboratory characterization of the velocity field in the FDA blood pump model using particle image velocimetry (PIV). *Cardiovasc. Eng. Technol.* 9(4):623–640, 2018. https://doi.org/10.1007/s13239-018-00378-y.
24. Peer, S. M., C. Yildirim, M. Desai, K. Ramakrishnan, P. Sinha, R. Jonas, et al. Mechanical support of pulmonary blood flow as a strategy to support the Norwood circulation-lumped parameter model study. *Eur. J. Cardiothorac. Surg.* 2022. https://doi.org/10.1093/ejcts/ezac262.
25. Williams, A. A. The turbine performance of centrifugal pumps: a comparison of prediction methods. *Proc. Inst. Mech. Eng. A J. Power Energy.* 208(1):59–66, 1994. https://doi.org/10.1243/pime_proc_1994_208_009_02.
26. Gülich, J. F. Pump hydraulics and physical concepts. In: Centrifugal Pumps, Berlin, Heidelberg: Springer, 2010, pp. 69–144.
27. Gibson, A. H., and J. E. Petavel. On the flow of water through pipes and passages having converging or diverging boundaries. *Proc. R. Soc. London Ser. A Contain. Papers Math. Phys. Character.* 83(563):366–378, 1910. https://doi.org/10.1098/rspa.1910.0025.

28. Coppage, J., F. Dallenbach, H. Eichenberger. Study of Supersonic Radial Compressors for Refrigeration and Pressurization Systems. Wright Air Development Center, 1956.
29. Johnston, J., and R. Dean Jr. Losses in vaneless diffusers of centrifugal compressors and pumps: analysis, experiment, and design. *J. Eng. Power.* 88:46, 1966.
30. Aungier, R. H. Mean streamline aerodynamic performance analysis of centrifugal compressors. *J. Turbomach.* 117(3):360–366, 1995.
31. Jansen, W. A method for calculating the flow in a centrifugal impeller when entropy gradient are present. *Inst. Mech. Eng. Intern. Aerodyn.* 32:711, 1970.
32. Tuzson, J. Centrifugal Pump Design. Hoboken: Wiley, 2000.
33. Conrad, O., K. Raif, and M. Wessels. The Calculation of Performance Maps for Centrifugal Compressors with Vane-Island Diffusers. Performance Prediction of Centrifugal Pumps and Compressors, pp. 135–147, 1979.
34. Antaki, J. F., M. R. Ricci, J. E. Verkaik, S. T. Snyder, T. M. Maul, J. Kim, et al. PediaFlow Maglev ventricular assist device: a prescriptive design approach. *Cardiovasc. Eng.* 1(1):104–121, 2010. https://doi.org/10.1007/s13239-010-0011-9.
35. Gao, Y., M. Li, M. Jiang, Y. Zhang, C. Wu, and X. Ji. Hemolysis performance analysis and a novel estimation model of roller pump system. *Comput. Biol. Med.* 159:106842, 2023. https://doi.org/10.1016/j.compbiomed.2023.106842.
36. Khosroshahi, F. K., H. Ertürk, and M. M. Pınar. Optimization of spectrally selective Si/SiO2 based filters for thermophotovoltaic devices. *J. Quant. Spectrosc. Radiat. Trans.* 197:123–131, 2017. https://doi.org/10.1016/j.jqsrt.2017.01.030.
37. Yildirim, C., H. Erturk, K. Pekkan, S. Deniz, and E. C. Serefoglu. A novel method for hemodynamic analysis of penile erection. *Int. J. Impot. Res.* 34(1):55–63, 2022. https://doi.org/10.1038/s41443-020-00362-y.
38. Stepanoff, A. J. Centrifugal and Axial Flow Pumps: Theory, Design, and Application. Krieger Publishing Company, 1993.
39. Ucak, K., F. Karatas, and K. Pekkan. Effect of impeller rotational phase on the FDA blood pump velocity fields. *Artif. Organs.* 2024. https://doi.org/10.1111/aor.14811.
40. OpenFOAM v2412 2024. https://www.openfoam.com/news/main-news/openfoam-v2412.
41. Menter, F. R., M. Kuntz, and R. Langtry. Ten years of industrial experience with the SST turbulence model. *Turbul. Heat Mass Trans.* 4(1):625–632, 2003.
42. Ghirelli, F., and B. Leckner. Transport equation for the local residence time of a fluid. *Chem. Eng. Sci.* 59(3):513–523, 2004. https://doi.org/10.1016/j.ces.2003.10.013.
43. Faghih, M. M., and M. K. Sharp. Modeling and prediction of flow-induced hemolysis: a review. *Biomech. Model. Mechanobiol.* 18(4):845–881, 2019. https://doi.org/10.1007/s10237-019-01137-1.
44. Miccoli, C., B. Collins, A. Scardigli, and F. Gallizio. Robust shape optimization of the FDA blood pump. *Meccanica.* 2024. https://doi.org/10.1007/s11012-024-01828-9.
45. CentriMag™ Blood Pump Instructions For Use (IFU). Abbot Medical, 2019.
46. Wang, L., S. N. Asomani, J. Yuan, and D. Appiah. Geometrical optimization of pump-as-turbine (PAT) impellers for enhancing energy efficiency with 1-D theory. *Energies.* 13(16):4120, 2020.
47. Wiegmann, L., B. Thamsen, D. de Zelicourt, M. Granegger, S. Boes, M. Schmid Daners, et al. Fluid dynamics in the HeartMate 3: influence of the artificial pulse feature and residual cardiac pulsation. *Artif. Organs.* 43(4):363–376, 2019. https://doi.org/10.1111/aor.13346.
48. Khamooshi, M., M. Azimi, and S. D. Gregory. Computational analysis of thrombosis risk with variations in left ventricular assist device inflow cannula design in a multi-patient model. *Comput. Methods Program. Biomed.* 240:107730, 2023. https://doi.org/10.1016/j.cmpb.2023.107730.
49. Hsiao, H. M., C. T. Yeh, Y. H. Chiu, C. Wang, and C. P. Chen. New clinical failure mode triggered by a new coronary stent design. *Biomed. Mater. Eng.* 24(1):37–43, 2014. https://doi.org/10.3233/BME-130781.
50. Kung, E., G. Pennati, F. Migliavacca, T. Y. Hsia, R. Figliola, A. Marsden, et al. A simulation protocol for exercise physiology in Fontan patients using a closed loop lumped-parameter model. *J. Biomech. Eng.* 136(8):0810071–08100714, 2014. https://doi.org/10.1115/1.4027271.
51. The Right Beat. Optimizing RVADs for Right Heart Failure Patients. Enschede, The Netherlands: European Society of Artificial Organs, 2025.
52. Escher, A., E. J. Hubmann, B. Karner, B. Messner, G. Laufer, U. Kertzscher, et al. Linking hydraulic properties to hemolytic performance of rotodynamic blood pumps. *Adv. Theory Simul.* 5(9):2200117, 2022. https://doi.org/10.1002/adts.202200117.
53. İncebay, Ö., and R. Yapici. Optimization of a centrifugal blood pump in terms of hemolysis index and hydraulic efficiency. *J. Brazil. Soc. Mech. Sci. Eng.* 46(10):603, 2024. https://doi.org/10.1007/s40430-024-05185-2.

Publisher's Note Springer Nature remains neutral with regard to jurisdictional claims in published maps and institutional affiliations.